ORIGINAL PAPER

physica **pss**a
status
solidi
www.pss-a.com

Check for updates

Intrapore-Texturized Vanadia-Hydrate Supercapacitor with Ultrahigh Area-Normalized Capacitance

Ying-Chu Chen,* Jens Treptow, Yu-Kuei Hsu, and Claus Feldmann*

A pressing need for ultrahigh area-normalized capacitance emerges from the migration to miniaturized composite supercapacitors. Herein, an advanced electric field-assisted sol–gel synthesis protocol that allows to obtain ribbon-like vanadium oxides that preferentially creep along the porous tunnels in a commercially available carbon host of low density is demonstrated. In particular, this design offers 1) to convert the original submicrometer-sized pore network into hierarchically macroporous yet 3D-interconnected bicontinuous composite frameworks and 2) to considerably add pseudo-capacitive functionalities onto a highly conductive carbon cloth backbone. Both are demonstrated by an unprecedented area-normalized capacitance exceeding 5 F cm^{-2}. Moreover, the as-designed symmetric supercapacitor is characterized by a maximum area-normalized cell capacitance in the order of 1 F cm^{-2}, a geometric energy density of 0.34 mW h cm^{-2}, and a geometric power density of 28.3 mW cm^{-2}. These features outperform commercial double-layer supercapacitors as well as many state-of-the-art composite pseudo-capacitors and lithium-ion microbatteries.

1. Introduction

Since 1996, the globally burgeoning transformation of power systems from central generation to local self-supply systems has been triggering an intensive and pressing need to establish compact elements for energy storage.[1] A concurrently increasing demand for augmented functionalities of ubiquitous portable electronics requires an enhanced density not only of on-board modules but also of power units that are both miniaturized and energy dense.[2] Composite supercapacitors emerge as appealing candidates to realize the relevant module dimensions.[3]

Dr. Y.-C. Chen, J. Treptow, Prof. C. Feldmann
Institut für Anorganische Chemie
Karlsruhe Institute of Technology (KIT)
Engesserstraße 15, 76131 Karlsruhe, Germany
E-mail: ying-chu.chen@kit.edu; claus.feldmann@kit.edu

Prof. Y.-K. Hsu
Department of Opto-Electronic Engineering
National Dong Hwa University
Hualien 97401, Taiwan

The ORCID identification number(s) for the author(s) of this article can be found under https://doi.org/10.1002/pssa.201900558.

The combination of transition metal oxides (TMOs) or conducting polymers (CPs) and carbonaceous materials, which are responsible for a rapid surface-allocated Faradaic (pseudo-capacitance) and non-Faradaic (electric double-layer capacitance, EDLC) charge storage, enables a composite supercapacitor to readily meet the diverse energy and power requirements in electronics,[4] with gradual differentiation between supercapacitors and batteries.[5]

Although the invariants of performance relate to high energy and power delivery, the conventional approach to estimate the performance only by normalization on the mass of the active material is not sufficient any longer.[6] More detailed considerations based on the effective area (footprint) and the volume of full modules become much more important in terms of the limited space for component installation in electronic modules. Remarkable progress regarding the volumetric performance has been demonstrated for micro-supercapacitors by reconfiguring the module structure, for instance, by decreasing the separation between antipodal electrodes to the microscopic level to ensure a spectacular power outcome that benefits from the shortened ionic transport.[2c,7] Additional efforts in patterning electrodes in a planar interdigitated geometry and in depositing them side by side rather than face-to-face resulted in a maximization of the energy capacity without increasing the module volume.

Nevertheless, the above superior properties per unit volume typically fail if the performance is normalized on the electroactive area. Hence, a total area on the millimeter scale (or even centimeter scale) and at least 1000 times the thickness of the microcapacitor is inevitable at the current state of the art to power additional integrated gadgets. The poor performance, if normalized to area, can impede their adoption in the emerging area of self-powered wireless systems, implanted with an enormous number of sensors that require power modules of large-area performance to drive those micrometer- or nanometer-sized units to allow an efficient management of common actions.[8] In this regard, a rapid response and a reliable performance is thus evitable to develop a composite supercapacitor that exhibits high energy density per device footprint.

The poor performance normalized to area is a long-standing issue for composite supercapacitors, even if the dimension of modules is decreased from the macroscopic to the microscopic scale, which virtually originates from a deficient areal packing density.[2c,6a] Although the active material, prepared in a

geometry analogous to a dense film, bears the greatest areal packing density, only the superficial phase is in direct contact with the electrolyte and contributes to the charge storage. Its extent strongly relates to the storage mechanism, which depends on the thickness that is generally in the order of few nanometers. In this regard, active materials are prepared as ultrathin films in state-of-the-art composite microcapacitors to maximize storage efficiency. Nevertheless, this comes at the expense of the footprint-normalized capacitance, which in turn demands a large areal occupancy of such microscopic energy supply units to power additional on-board gadgets in portable multifunctional electronics. To address these issues, the prevalent strategy nowadays is to transform the electrode structure from a traditional 2D planar geometry to a 3D hierarchical nanoarchitecture using solid matter in the available module volume.[3b,c,e,f,9] This modification aims at reinforcing the fraction of active material per module footprint while effectively exposing it to the electrolyte to promote the overall performance.

The electrode engineering typically includes the use of carbonaceous substances to establish a 3D-interconnected porous framework, followed by the decoration of the internal walls with TMOs or CPs. In this regard, Long and coworkers and Kaner and coworkers, as prominent examples, demonstrated impressive areal performances of 0.85 and 2.5 F cm^{-2} for MnO$_2$-based systems in two- and three-electrode configurations, respectively.[3b,f] However, these results were nonoptimal in terms of the frustrated implant efficiency of MnO$_2$. Thus, a thick crust atop the underlying carbonaceous scaffold was invariably present, which mostly originated from an inappropriate pore size distribution (including mesopores of 2–50 nm and abnormally small macropores of few hundreds of nanometers), which obstructed the infiltration of functional MnO$_2$ throughout the porous network. This dense envelope did not only block the pores for electrolyte penetration but also imposed an undesirable charge-transfer resistance on the resulting composites, which impedes the areal capacitance.[10] As a sufficient areal performance is a prerequisite toward next-generation nanocapacitors, it is crucial to address the way of packing of the active oxide on the conductive carbon host.

With this work, we propose an innovative integration protocol that reforms the traditional hybridization recipe for the first time. In particular, our electrode design lies in an enhanced freedom to grow the active oxides, which independently establish an additional framework to become integrated into a pre-existing carbonaceous network via careful creeping along the porous tunnels inside of the preformed architecture. Such integration guarantees most of the pore volume to become efficiently filled by the active oxide instead of the electrolyte, which also increases the packing density. More importantly, the independent deposition of the oxide on the carbonaceous network ensures that complementary electroactive sites store charges via both Faradaic and non-Faradaic processes, which results in a remarkable footprint-normalized capacitance.

We have chosen a woven carbon cloth (CC) with a moderate pore distribution (free space of 2–4 μm between individual fibers and 10–30 μm between yarns) to realize a carbon-based host frame in terms of those macropores that facilitate the infiltration of additional functional materials to utilize intrapore texturization.[11] Moreover, the reliable commercial availability, the readily

tailored geometry, and the size for relevant applications render the CC to become a favorable carbonaceous ingredient in a composite supercapacitor.[9a] We have used vanadium pentoxide (V$_2$O$_5$) as a functional material to impart pseudo-capacitance in addition to the EDLC offered by the CC to the composite supercapacitor. In particular, V$_2$O$_5$ holds great promise among abundant and environmentally benign TMOs because its characteristic layered structure ensures a large charge-storage capacity.[12] More importantly, the multiple stable oxidation states (from +III to +V) enable a wide working window spanning from a cathodic to an anodic potential range, which, combined with a moderate electrical conductivity (10^{-2}–10^{-3} S cm^{-1}), makes the delivery of great energy and power feasible.[13] As a result, a composite supercapacitor is arranged in a dual-textile configuration, in which V$_2$O$_5$ nanoribbons (NRs), trailed between adjacent fibers or yarns and intimately anchored to carbon struts, offer an unprecedented area-normalized capacitance up to 5.08 F cm^{-2}. Such areal capacitance is 58 times over the native CC and outperforms comparable, known materials with traditional coating-like packing by one order of magnitude.[12] Moreover, a symmetric module made of these electrodes exhibits a great energy density of 0.34 mW h cm^{-2}, comparable with that of lithium-ion microbatteries, but with a superior power density of 28.3 mW cm^{-2}, as well as satisfactory cycle stability.

2. Results and Discussion

To extract the augmented energy from the effective area of a composite supercapacitor, improvements in either the area-normalized capacitance or the operating voltage window are prerequisite.[6] In particular, the areal capacitance of a composite electrode is mainly dictated by pseudo-capacitive materials, namely, oxides or polymers. The essential charge-storage processes involve simultaneous insertion of electrons and cations, so that electrons move from the external circuit and along the conductive host into the active oxide, whereas cations migrate through the bulk electrolyte and across the interconnecting tunnels inside the electrode frame.[2e] With such working principles, the areal capacitance is expected to increase with the availability of active sites, at which the antipodal carriers meet. The conventional packaging prototype to treat these concerns is summarized in **Scheme 1**.

A large specific surface area inside a preformed carbonaceous nanoarchitecture provides more nucleation sites to increase the mass uptake of the active oxide and the concomitant pseudo-capacitance. However, these energetic surface sites concurrently accelerate the nucleation kinetics of the interior deposition process, in which a lateral merging of deposited clusters along the supporting backbone is promoted upon increasing the cluster density. The confined degree of freedom for deposition eventually leads to the formation of a coating analogous to a thin film and an oxide loading readily saturated at the depletion of nucleation sites. Moreover, the negative association between specific surface area and diffusion mobility of the feedstock in the preformed structure highlights a considerable challenge in further refining the functional oxides in quantity.[14] Overall, the saturation of oxide implantation using such a strategy reflects a limitation in translating the excellent mass-related properties of the
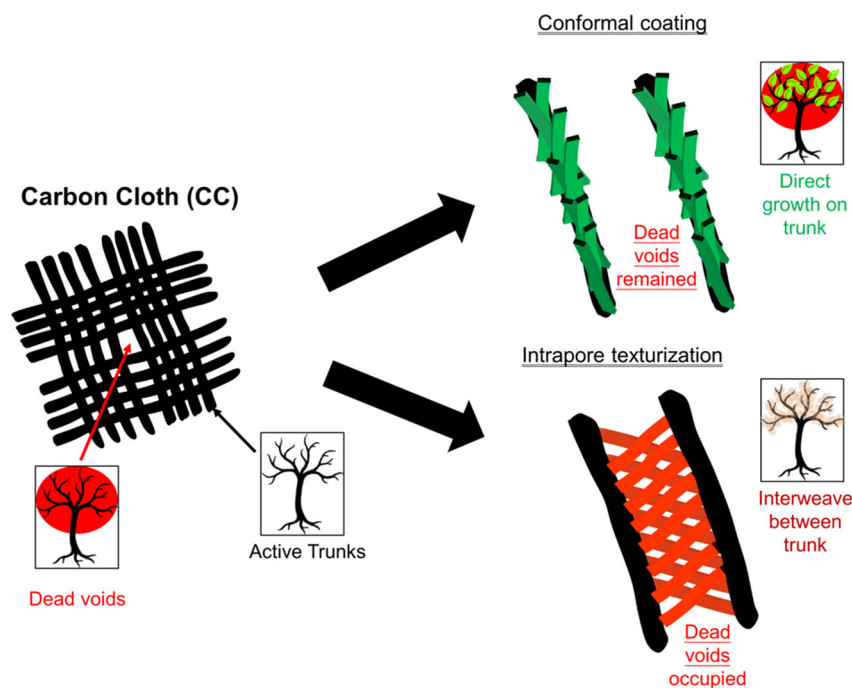
Scheme 1. Schematic illustration of conventional conformal coating and intrapore texturization strategies for the preparation of composite supercapacitor electrodes.

active oxide to the overall area-normalized characteristics of the composite electrode.

An option to integrate considerably more pseudo-capacitive materials into supercapacitors relates to increasing the degree of freedom in terms of a material growth, thus, instead of two dimensions (e.g., deposition along the framework surface) to three dimensions (i.e., growth in the empty volume between adjacent scaffolds), as shown in Scheme 1. The ample free space of the pores can avoid the lateral fusion of the active oxide due to spatially increased degree of freedom of the isotropic growth and preserves the nanostructure of the active oxide, which promotes more active sites to be accessible for both antipodal carriers. To realize such additional degree of freedom, the implantation of the active oxide—conventionally involving redox reactions between ingredients and the host framework—must be translated from the surface of the scaffold to the space between the scaffolds.[3f] In particular, this transfer includes an additional mediator to shuttle the charge and the inert ingredients without any competition for charges but with a great selectivity to react exclusively with the mediator.

Our work tackles the above challenge by using ammonium metavanadate ($NH_4V^{+V}O_3$) to obtain vanadium pentoxide (V_2O_5) (further details of synthesis are given in Figure S1–S7, Supporting Information). In view of the equal oxidation state of V in $NH_4V^{+V}O_3$ and $V_2^{+V}O_5$, the charge conflict can be avoided. In addition, the omnipresent water plays a key role in adjusting the position of V_2O_5 nucleation. The reaction was triggered with the aid of a galvanostatic technique and a positive current. Given the highest oxidation state of vanadium (V^{V+}) in the hydrated precursor, the excessive holes solely consume ubiquitous OH^- ions and result in an abrupt decrease in the local pH

at the conductive CC host. The unreacted protons (H^+) in turn compensate the negative charge on the hydrated V^{v+} species and bring them to a point of zero charge (PZC) to generate neutral, solid V_2O_5.[15] Benefiting from this watery shuttle, polycondensation within the V_2O_5 host occurs in voids rather than at the surface. This is evidenced by scanning electron microscopy (SEM) images as a function of the elapsed time during synthesis (Figure S5, Supporting Information). The molecular structure of the hydrated precursor turned out as essential in regard to the morphology of the resulting V_2O_5 precipitation. Thus, the molecular shape not only depends on the pH but also on other solvated species in the solution. The presence of SO_4^{2-} anions plays another crucial role in establishing the as-obtained NR morphology.

A closer inspection by top-view and cross-sectional SEM images in **Figure 1**a and Figure S6, Supporting Information, evidently reveals that functional V_2O_5 is implanted homogeneously over the entire fibrous network (inset in Figure 1a). Moreover, V_2O_5 is distributed mostly within the interfiber voids, as highlighted in the inset of Figure 1b. Prima facie, the ample free space within these intrapores offers an additional degree of freedom to the infusion of V_2O_5 into the CC host. In turn, this allows to circumvent the lateral merging of V_2O_5 and maintain the nanostructure even at high mass ratios (vanadium oxide-to-host CC) of more than 2.5. Figure 1c shows the typical geometric features of V_2O_5 that is in the form of NRs with thicknesses of few nanometers and diameters up to hundreds of nanometers (about 300 nm on average) and lengths up to tens of micrometers. Even more important, the V_2O_5 NRs are highly texturized, forming a porous yet continuous network, as punctuated in Figure 1b. It should be noted that this microtexture differs significantly from that reported in the literature, wherein an
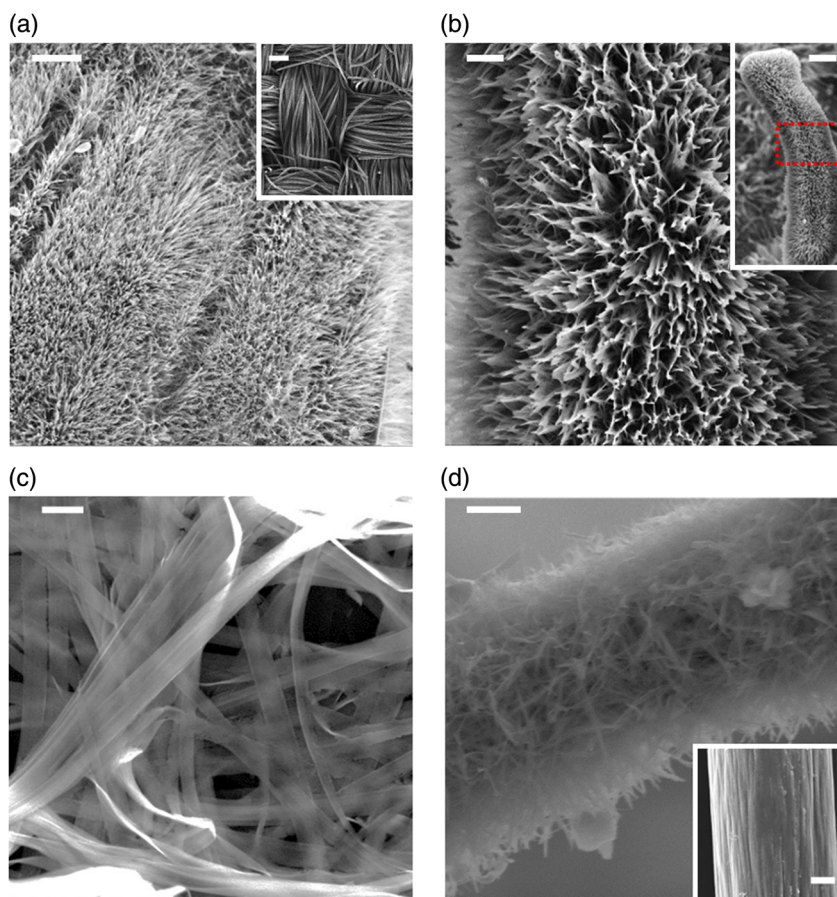
Figure 1. Top-view SEM images illustrate a) the spatially homogeneous integration of $V_2O_5 \times H_2O$ (scale bar: 5 µm) into the CC (inset, scale bar: 100 µm), b) $V_2O_5 \times H_2O$ precipitates mostly in the voids (scale bar: 5 µm) between adjacent carbon fibers (performed at the framed region in the inset, scale bar: 50 µm), c) ribbon-analogous morphology (scale bar: 500 nm) of the $V_2O_5 \times H_2O$ deposits, d) additional distribution of $V_2O_5 \times H_2O$ over (scale bar: 5 µm) individual carbon struts (inset, scale bar: 2 µm).

undesirable mutual stacking of the V_2O_5 NRs was typically obtained via hydrothermal synthesis.[12a,15,16] This specific microstructure in combination with the featured ribbon-like nanostructure is in favor of a fluent ion diffusion into V_2O_5. As the charge storage is completed when ions meet the electrons in V_2O_5, a rigid path for electron transport is also nontrivial. This issue has been also addressed with the present electrode design, at first offering intact junctions between the V_2O_5 forest and the underlying carbon struts to endow electrons with a kind of "superhighway". This path is established at the earliest stage of charge being transferred from the host carbon fibers to the water mediators. A surface activation, involving the breaking of originally hydrophobic C—C bonds and introducing carboxylic (—COOH) and hydroxyl (—OH) groups, occurs simultaneously to the oxidation of water. These functional groups participate not only in delivering holes for O_2 generation but also lead to nucleophilic attacks of the highly charged V^{5+} ions and promote a deposition at the surface, as emphasized in Figure 1d.

High-resolution transmission electron microscopy (HRTEM) images provide additional insights into the structural order, giving clues to electron delivery along individual NRs. A quasi-intact lattice frame with fringes aligned unidirectionally across the

entire photographed section indicates the V_2O_5 NRs to be crystalline (**Figure 2**a). Such a long-range lattice order is further reinforced by the conspicuous diffraction peaks seen in the collected X-ray diffraction (XRD) pattern (Figure 2b), altogether corroborating a successfully established "superhighway" for electron movement. Moreover, the XRD results in addition suggest that the V_2O_5 NRs are in its hydrated form with all Bragg peaks readily indexed to $V_2O_5 \times H_2O$ (ICDD-No. 11-0673).

The presence of water in the crystal structure of the V_2O_5 NRs are further ascertained by Raman spectroscopy and specifically by the ≈ 440 cm^{-1} mode (upward arrow, Figure 2c) that originates particularly from the liberation motion of water.[17] In addition, the stretching vibration of the vanadyl bond (V=O) and the displacement between individual lamellae that build up the layered V_2O_5 lattice give rise to the Raman bands at 117, 139, and 1005 cm^{-1}, respectively.[18] In contrast to the well-defined spectral profile of these Raman lines, the vibrational modes at 250–300 and ≈ 690 cm^{-1} that relate to the rocking oscillation of V=O bonds and the stretching vibration of the V—O bond are highly diffuse (downward arrows, Figure 2c). Such band-like line shapes were reported to originate from the fluctuation in the vibrations of V—O and V=O bonds due to the coordination with

ADVANCED
SCIENCE NEWS
www.advancedsciencenews.com

physica
pss status
solidi a

www.pss-a.com
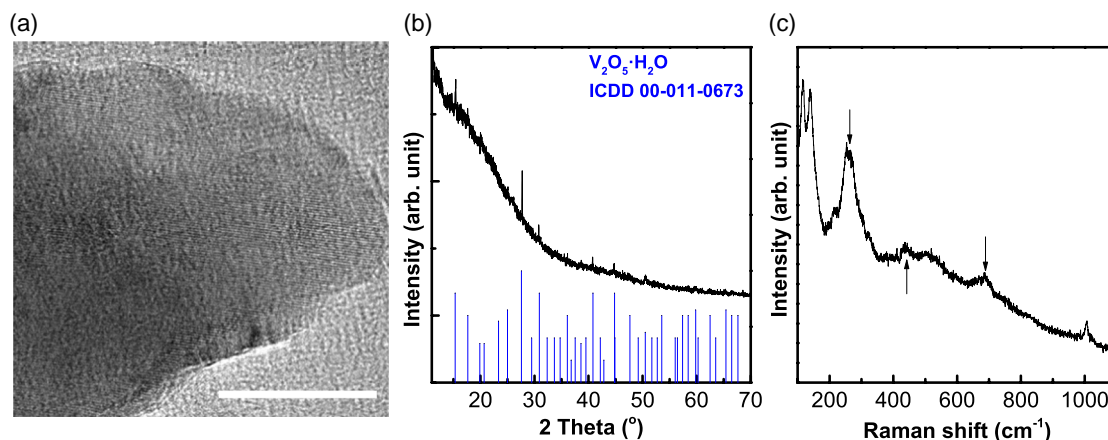
Figure 2. a) HRTEM image reveals quasi-continuous lattice fringes along individual $V_2O_5 \times H_2O$ NRs (scale bar: 20 nm), b) XRD pattern, and c) Raman spectrum of the as-grown $V_2O_5 \times H_2O/CC$ electrode. The assignments of the vibrational modes are defined in the text.

water and specifically if water is trapped in cavities between the lamellar V_2O_5 slabs.[19] This evidently validates crystal water to be present in the interlayer gallery of V_2O_5 and leads to its swelling.[20] This finding, along with the highly porous microtexture originating from intrapore texturization, not only allows an efficient contact between V_2O_5 and the electrolyte, but even more importantly also favors the ion diffusion and intercalation into V_2O_5, which in turn successfully trigger its pseudo-capacitance, as elucidated later.[20,21]

The electrochemical properties of the $V_2O_5 \times H_2O$ NRs were evaluated in a three-electrode configuration using LiCl aqueous solution (5 M) as the electrolyte, a Pt foil as the counter-electrode, and Ag/AgCl as the reference electrode. **Figure 3**a shows a cyclic voltammogram (CV) recorded for the $V_2O_5 \times H_2O/CC$ electrode with a potential window of -0.2 and $+0.8$ V versus Ag/AgCl (KCl 3 M, 0.207 V vs SHE) at a scan rate of 5 mV s^{-1}. For the sake of comparison, additional CV results of other samples including CC electrodes without and with vanadium oxide (VO$_x$) NRs, which were exclusively carpeted upon fibers by other measures (Figure 3a), are plotted in parallel.[12a,15,16] In this study, a significantly enhanced area under the CV curve was first perceived after imbuing the bare CC with pseudo-capacitive functionalities. The redox behavior reveals the discrepancy in the working mechanisms, in which carbonaceous materials predominantly store charge by virtue of the EDLC. In particular, the $V_2O_5 \times H_2O/CC$ electrode manifests a CV curve area markedly augmented relative to VO$_x$/CC, despite the fact that both function on an equivalent working basis. The area-normalized capacitance of the $V_2O_5 \times H_2O/CC$ electrode reaches an order of F cm^{-2} rather than mF cm^{-2} with 3.05 F cm^{-2} at 5 mV s^{-1}. This value exceeds that of the VO$_x$/CC electrode under identical conditions of measurement almost by a factor of seven (**Table 1**).

In fact, an unprecedented capacitance of 5.08 F cm^{-2} is reached with the $V_2O_5 \times H_2O/CC$ electrode at 0.1 mV s^{-1}. To the best of our knowledge, such value is the highest in terms of area-normalized capacitance that was reported for hybrid electrodes using active oxides with a featured operation potential window of $\approx$1 V, corresponding to the nominal thermodynamic

tolerance of water.[3a,b,e,f,12a,18] In addition, the capacitance is 58 times that of the native CC, which also demonstrates the advantage of the present protocol as shown in Figure 3b. In view of CC primarily relying on EDLC for charge storage, the obtained capacitance (52.1 mF cm^{-2}) reflects an effective surface area available for ion accumulation.

Figure 3b shows additional carbonaceous materials that were reported as host frames in composite electrodes to obtain superior areal performances after oxide implantation. This includes carbon nanofoams (CNFs) and laser-induced graphene (LIG).[3a,b,f,9a,10,18] CNFs and LIG stand at opposite ends with CC positioned in between in terms of areal capacitance. The discrepancies mostly arise from the distinct size distribution of macropores but also partially from varying thickness and measurement configurations (further details of porosity-, geometry-, and electrode configuration-dependent capacitance given in Figure S8, S9 and Table S1, S2, Supporting Information). A capacitance depending on the pore size clearly highlights the issue of over-tailoring the architecture of carbonaceous matter in a conventional protocol. Those abnormally small macropores—as a side effect of the structural adaption of LIG and CNF—lead to a large specific surface area but impair the entry of ions, resulting in an impractically small capacitance (<1 mF cm^{-2} for LIG), less feedstocks, and a limited enhancement (merely $\approx$1 F cm^{-2} after oxide implantation). We have used the pristine CC directly without intricate and tedious pretreatment to eliminate these harsh conditions. Even more importantly, the dual-textile electrode design with carefully deposited functional $V_2O_5 \times H_2O$ NRs in the larger macropores of the CC prevents the idleness of the porous tunnels that preferentially serve as electrolyte reservoirs. The appreciably enhanced pseudo-capacitance (i.e., more than $\approx$3 F cm^{-2} after oxide implantation) and the benchmarked overall capacitance clearly reveal the settlement of the deficient integration efficacy based on our recipe.

As another feature, the $V_2O_5 \times H_2O/CC$ electrode exhibits a robust rate capability that sustains diverse scan rates (Figure 3c). The consecutive redox behavior becomes invariably visible if the scan rates were increased by a factor of 10, indicating an efficient response of ion diffusion and intercalation to
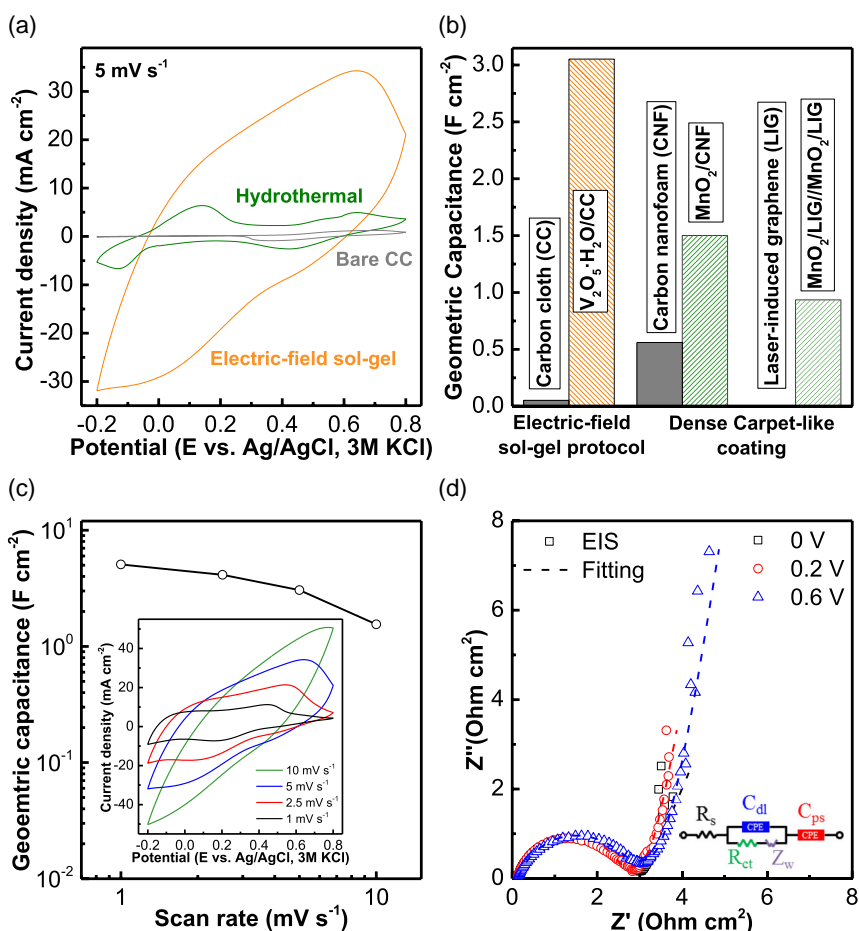
Figure 3. a) CVs of native CC electrodes before (grey line) and after imparting pseudo-capacitive functionalites with vanadium oxide via hydrothermal coating (green line) and electrochemical intrapore texturization (orange line) methods. b) Area-normalized capacitances of native CC electrode and composite $V_2O_5 \times H_2O/CC$ electrode derived from CVs in aqueous LiCl electrolyte at a scan rate of 5 mV s^{-1} (with state-of-the-art composite super-capacitor electrodes with excellent area-normalized capacitances plotted alongside for comparison). c) Area-normalized capacitance of the composite $V_2O_5 \times H_2O/CC$ electrode as a function of the scan rate. Inset: CVs of composite $V_2O_5 \times H_2O/CC$ electrodes at diverse scan rates. d) Nyquist plots of the $V_2O_5 \times H_2O/CC$ electrode recorded in aqueous LiCl electrolyte over a frequency range of 10 kHz–0.01 Hz.

the increased electron flux under high-rate operations. The $V_2O_5 \times H_2O/CC$ electrode continuously provides a capacitance in the order of F cm^{-2} with 1.55 F cm^{-2} as the highest rate that nearly tripled the performance of state-of-the-art $V_6O_{13-x}S_x/CC$ electrodes at the same scan rate.[12a] Such a superior rate capability of the $V_2O_5 \times H_2O/CC$ electrode can be ascribed to the abundant addressable surface area of the $V_2O_5 \times H_2O$ nanoforest for ions and the small internal resistance as a result of the high crystallinity and the direct contact between the carbon fibers and the $V_2O_5 \times H_2O$ NRs.

To rationalize the origin of the exceptional electrochemical properties of the $V_2O_5 \times H_2O$ NRs, we have performed a more elaborate analysis, relying on electrochemical impedance spectra (EIS) to allow a quantitative characterization (Figure 3d). The Nyquist plots of the $V_2O_5 \times H_2O/CC$ electrode were recorded at various voltages with a perturbation of 10 mV over a frequency range of 10 kHz–0.01 Hz. Quantitative analyses (**Table 2**) were also performed for these impedance spectra using a fitting method (i.e., complex nonlinear least squares, CNLS) based

on an equivalent circuit shown in the inset of Figure 3d.[22] Upon negative polarization, electrons accumulate on the $V_2O_5 \times H_2O/CC$ electrode at a decreasing oxidation state of vanadium.[12a,23] In general, such a Faradaic process is coupled with an intercalation of counter-ions (Li$^+$) into the lamellar tunnels of the $V_2O_5 \times H_2O$ NRs for electroneutralization.[6b] As the potential was continuously swept downward, more vanadium was proceedingly involved in the Faradaic transition. As a consequence, the increased diffusion time coefficient (τ_d) indicates an extended diffusion path of Li$^+$ to compensate the negative charges stored at the interior vanadium sites.

Additional clues to these Faradaically stored electrons, efficiently offset by the intercalated Li$^+$, are manifested in the increased pseudo-capacitance (C_{ps}), the decreased diffusion (R_w), and charge-transfer resistance (R_{ct}) at lower voltages. A closer inspection reveals a slight increment in the solution resistance (R_s), which accounts for an ionic resistance of the electrolyte, the intrinsic and interfacial resistance of the $V_2O_5 \times H_2O$ NRs, and the underlying CC host, simultaneously. This situation

Table 1. Overview of area-normalized capacitances of state-of-the-art composite supercapacitor electrodes in aqueous electrolyte.

Electrode	Electrolyte	Potential window	Mass uptake	Areal capacitance [mF cm^{-2}][h]
Three-electrode configuration				
VO_x/CC	5.0 M LiCl	−0.2–0.8 V[e]	1.1 mg cm^{-2}	438 (5 mV s^{-1})
$V_6O_{13-x}S_x/CC$[11a]	5.0 M LiCl	0–1 V[f]	1.9 mg cm^{-2}	720 (1 mA cm^{-2})
				560 (10 mV s^{-1})
$RuO_2 \times H_2O/Au$[3e]	0.5 M H_2SO_4	0.05–0.9 V[f]	Not reported	3250 (0.1 mV s^{-1})
MnO_2/CNF[3f]a]	2.5 M Li_2SO_4	0–1.1 V[e]	60%[g]	2500 (2 mV s^{-1})
FeO_x/CNF[21b]a]	2.5 M Li_2SO_4	−0.8–0.2 V[e]	17%[g]	850 (5 mV s^{-1})
$V_2O_5 \times H_2O/CC$	5.0 M LiCl	−0.2–0.8 V[e]	30 mg cm^{-2}	5081 (1 mV s^{-1})
Two-electrode configuration				
$MnO_2/LIG//MnO_2/LIG$[3a]b]	PVA/LiCl	0–1 V	Not reported	934 (0.5 mA cm^{-2})
$PANI/LIG//PANI/LIG$[3a]b]	PVA/H_2SO_4	0–0.8 V	Not reported	361 (0.5 mA cm^{-2})
$MnO_2/LSG//MnO_2/LSG$[3b]c]	1 M Na_2SO_4	0–0.9 V	≈6 mg cm^{-2}	852 (1 mV s^{-1})
$RuO_2 \times H_2O//RuO_2 \times H_2O$[3e]	PVA/SiWa[d]	0–0.9 V	Not reported	1220 (1.5 mA cm^{-2})
$V_2O_5 \times H_2O//V_2O_5 \times H_2O$	5.0 M LiCl	0–1 V	60 mg cm^{-2}	1223 (10 mA cm^{-2})

[a]Carbon nanofoam (CNFs); [b]Laser-induced graphene (LIG); [c]Laser-scribed graphene (LSG); [d]Silicotungstic acid (SiWa); [e]Versus Ag/AgCl; [f]Versus SCE; [g]Mass percent derived from active oxides normalized to the underlying carbon host; [h]A factor of 2–4 in area-normalized capacitance between three- and two-electrode configurations should be taken into account.[9,10]

Table 2. Results of fits of impedance spectra.

Potential [V]	R_s[a]	C_{dl}[a]	R_{ct}[a]	R_w[a]	τ_d[a]	C_{ps}[a]
0.6	0.12	2.55	2.57	1.11	2.26	2.10
0.2	0.13	1.17	2.44	1.11	5.49	4.09
0	0.13	0.76	2.44	1.07	5.73	4.91

[a]R_s [Ω cm^2]: solution resistance; R_{ct} [Ω cm^2]: charge-transfer resistance; R_W [Ω cm^2]: diffusion resistance; τ_d [s]: diffusion time coefficient; and C_{dl} [mF cm^{-2}] and C_{ps} [F cm^{-2}]: double-layer and pseudo-capacitance.

implies that the insertion of Li$^+$ induces more or less mechanical strain in the $V_2O_5 \times H_2O$ NRs,[16] but—given the insignificant influence on R_s—we believe that the marginal grain boundaries at the surface region of the $V_2O_5 \times H_2O$ NRs effectively mitigate the structural stress.

To substantiate the capacitive performance of the $V_2O_5 \times H_2O/CC$ electrode on a module level, we have assembled a symmetric supercapacitor (SSC) by sandwiching two $V_2O_5 \times H_2O/CC$ electrodes with LiCl as the electrolyte. The electrochemical characteristics of this $V_2O_5 \times H_2O$ SSC module was evaluated with CV and galvanostatic charge and discharge (GCD) methods and voltages swept between 0 and 1 V. At first sight, the recorded CV curve is featureless but broad and quasi-rectangular (**Figure 4**a), which proves the $V_2O_5 \times H_2O$ SSC module to serve as a capacitor. Such a conclusion is confirmed by the featured GCD profile of the $V_2O_5 \times H_2O$ SSC (inset in Figure 4b), wherein the charge accumulation and release phenomena quasi-linearly depend on the potential. Moreover, the mutual shape of the charging and discharging curves persisting in every GCD cycle at different current densities implies a great coulombic efficiency of the $V_2O_5 \times H_2O$ SSC independent of the rate,

even though a discernible IR drop appears when the current polarity is switched. The emerging Ohmic drop can be attributed to an augmented serial resistance due to the adaptation of the cell configuration. The module capacitance of the $V_2O_5 \times H_2O$ SSC evaluated according to aforementioned techniques is shown in Figure 4b. In particular, the best result of 1.22 F cm^{-2} was obtained for the $V_2O_5 \times H_2O$ SSC at a current density of 10 mA cm^{-2}, which is comparable to the best results of a recently reported SSC based on highly conductive hydrous ruthenium dioxide ($RuO_2 \times xH_2O$) that, however, was collected at a low current density of 1.5 mA cm^{-2} (Table 1).[3e] Even higher performance values can be achieved but typically require more sophisticated, more complex, and/or less stable materials such as graphene aerogels, carbon nanotube composites, and porous NiCoP nanowalls.[24]

The cycling performance of charging and discharging the $V_2O_5 \times H_2O$ SSC was explored over 10 000 cycles (Figure 4c). Here, a typical LiCl/PVA gel electrolyte was used for stability evaluation, so an irreversible dissolution of vanadium oxide was efficiently alleviated.[12b,16] A minor increase in the area-normalized capacitance in the initial cycles appeared, which most likely originates from the activation of the $V_2O_5 \times H_2O/CC$ electrodes. Altogether, more than 90% of the original capacitance was retained after 10 000 cycles, indicating that the neutral gel medium, coupled with characteristic superficial grains in the $V_2O_5 \times H_2O$ NRs, quenches undesired chemical and mechanical fading of the module capacitance. The overall performance of the $V_2O_5 \times H_2O$ SSC is summarized in a Ragone plot depicting the relation between energy and power delivery. The yardstick of this Ragone plot considerably deviates from a conventional gravimetric energy and power density. That performance is expressed after normalizing to an effective module footprint in the Ragone plot, which is in practice meaningful as the available estate in electronics to integrate
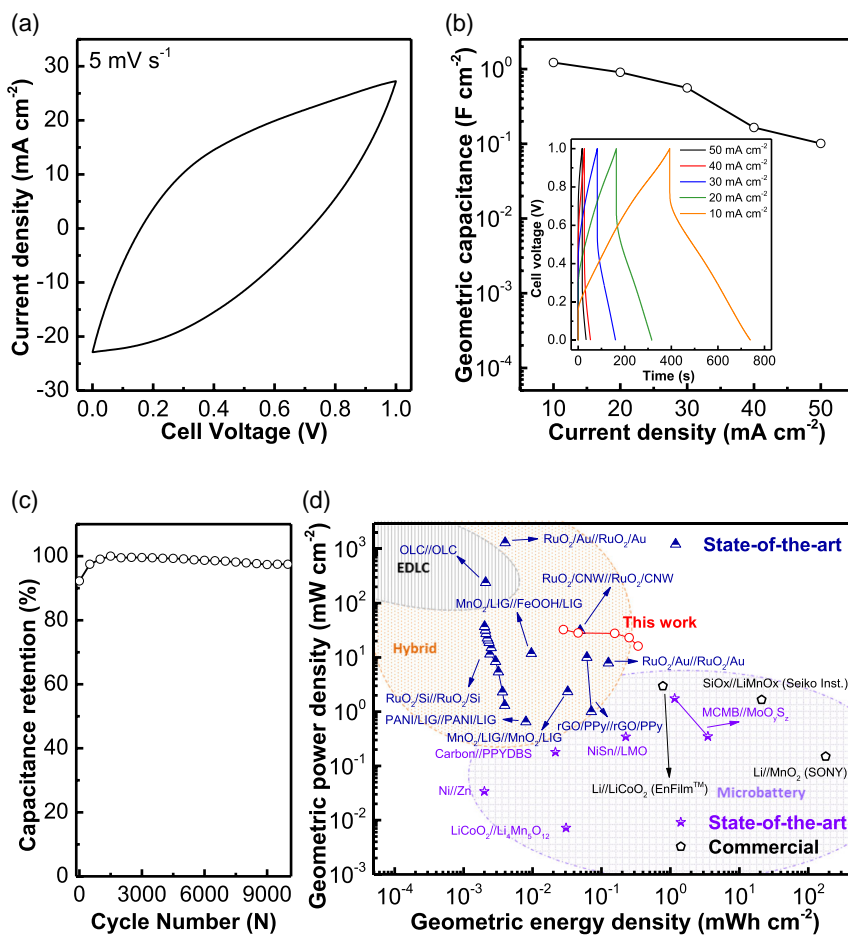
Figure 4. a) CVs of the assembled symmetric $V_2O_5 \times H_2O/CC$ supercapacitor in LiCl electrolyte recorded with a voltage window of 1 V at a scan rate of 5 mV s^{-1}. b) Area-normalized capacitance of the assembled symmetric $V_2O_5 \times H_2O/CC$ supercapacitor derived from the GCD curves (inset) in LiCl electrolyte at varied current densities. c) Cycling performance of the $V_2O_5 \times H_2O/CC$ SSC in LiCl/PVA gel electrolyte measured at 40 mA cm^{-2} for 10 000 cycles. d) Ragone plots of the symmetric $V_2O_5 \times H_2O/CC$ supercapacitor (commercial and state-of-the-art supercapacitors and microbatteries plotted alongside for comparison).

components on board is limited. In comparison, additional promising modules including commercial and state-of-the-art submacro-, micro-supercapacitors, and microbatteries, which are specially designed and fabricated to serve in portable electronics, are plotted as well.[2f,3a-c,e,25] Remarkably, the $V_2O_5 \times H_2O$ SSC is positioned near the upper-right corner in the Ragone plot. In particular, the area-normalized energy density at small rates (10 mA cm^{-2}) reaches 0.34 mW h cm^{-2}. Accordingly, the $V_2O_5 \times H_2O$ SSC appears at the right side of EDLC, whereas the power delivery of 16.2 mW cm^{-2} pins the module on a similar order of magnitude as most of the hybrid elements (Figure 4d). Moreover, an area-normalized power density up to 28.3 mW cm^{-1} at a rate of 40 mA cm^{-2} coupled with an energy delivery of 0.04 mW h cm^{-2} renders the $V_2O_5 \times H_2O$ SSC to become situated well above microbatteries. This result is particularly encouraging in terms of the remarkable area-normalized performance that could readily meet energy and power demands of electronics with little areal occupancy. The most highly prized estate in a device is hence effectively saved to allow more gadgets to be loaded on board for extra augmentation of functionality.

3. Conclusion

For the first time, a long-standing issue in the realm of electrochemical energy storage in terms of a deficient areal packing density of active materials in a full module, which substantially hinders to translate the outstanding material characteristics into the module performance, has been resolved by a dual-textile protocol. In this work, the electric field-assisted sol–gel recipe allows $V_2O_5 \times H_2O$ to be loaded into a CC with a mass uptake up to 30 mg cm^{-2}, which represents the largest packing density in the fabrication of hybrid supercapacitors. Moreover, a well-defined microtexture—analogous to a forest—consisting of numerous $V_2O_5 \times H_2O$ NRs persists even at such a great population, which turned out as the key to transfer the material properties into module performance. Thus, superior area-normalized capacitances of 5.08 and 1.22 F cm^{-2} were obtained, coupled with an aqueous electrolyte in three- and two-electrode configurations, respectively. These characteristics are the highest values among the as-reported mainstream materials for hybrid supercapacitors. Even more importantly, an out module-ready

SSC gives rise to an outstanding area-normalized energy and power delivery with maxima of $0.34\,\mathrm{mW\,h\,cm^{-2}}$ and $28.3\,\mathrm{mW\,cm^{-2}}$, respectively. This work not only suggests an innovative packing strategy that could result in an energy-dense and performance-reliable module but also offers a great opportunity to researchers to further improve the present system by the further engineering of physicochemical properties of $V_2O_5 \times H_2O$ or scientists to exploit these properties in other material systems using the presented dual-textile protocol.

4. Experimental Section

Materials: CC (B-1, designation A: plain-weave, $116\,\mathrm{g\,m^{-2}}$, thickness 0.35 mm; no wet-proofing), functioning as a host material in the here-presented hybrid supercapacitor electrodes, was purchased (E-TEK Division, USA). Ammonium metavanadate (NH_4VO_3, $\geq$99%, Sigma-Aldrich) and anhydrous sodium sulfate (Na_2SO_4, 99%, Sigma-Aldrich) served as precursors for the preparation of monohydrated vanadium pentoxide ($V_2O_5 \times H_2O$). Vanadium oxides (VO_x) were otherwise prepared with ethanol (C_2H_5OH, $\geq$99.5%, Sigma-Aldrich), hydrochloric acid (HCl, 37%, Sigma-Aldrich), and ammonium metavanadate. All precursor solutions were prepared with deionized water of a resistivity not less than $18.2\,\mathrm{M\Omega\,cm}$. To evaluate the electrochemical properties, we used lithium chloride (LiCl, $\geq$99%, Sigma-Aldrich) as the starting material to prepare an aqueous supporting electrolyte. All chemicals used in this work were of analytical grade and used as received.

Preparation of $V_2O_5 \times H_2O$ Nanoribbon/CC Electrodes: CC serving as the host framework was first cut into pieces with a working area of 3×0.5 cm. Each of it was then attached with a copper wire at the short edge. The junction was next covered with silver paste to ensure a well-conducting circuit for the following electroplating. The connecting pad was coated with epoxide to prevent undesirable side reactions. After this pretreatment, the CC was subjected to electrodeposition on immersing into a precursor solution with a nominal area of $1\,\mathrm{cm^2}$. The precursor solution consisted of ammonium metavanadate (0.26 M), to which sodium sulfate was added as supporting electrolyte. A three-electrode configuration prepared with CC as the working electrode, a Pt foil as the counter-electrode, and a Ag/AgCl electrode in potassium chloride (KCl, 3 M) solution as the reference electrode was used for electrodeposition. The electroplating was performed at a constant current flow of $1.5\,\mathrm{mA\,cm^{-2}}$ for 12 h at 70 °C. For the synthesis reported here, the concentration of sodium sulfate was varied from 0 to 2 M. The as-grown specimens were rinsed several times with distilled water to remove all residual precursors before subjecting to vacuum drying. A potentiostat (CH Instruments, CHI 627D) was used for all electrodepositions and all subsequent electrochemical tests. The mass uptake of $V_2O_5 \times H_2O$ was determined with a microbalance (Sartorius BP 211D, Germany, accuracy 10 μg).

Preparation of VO_x Nanoribbon/CC Electrodes: VO_x/CC electrodes used in this work were synthesized via reported hydrothermal methods.[16] Ammonium metavanadate (0.486 g, 4.2 mmol) was dissolved in an aqueous ethanol solution (75 mL, volume ratio of 10% ethanol in water). The pH of the solution was adjusted to $\approx$2 with HCl. A piece of clean CC was immersed in the precursor solution, and the entire system was transferred to an autoclave (Teflon-lined, 100 mL). The autoclave was heated at 160 °C for 12 h, followed by natural cooling to 23 °C. The as-prepared VO_x/CC electrodes were rinsed several times with distilled water to remove all residual precursors before subjecting to vacuum to remove all moisture. The mass uptake of VO_x was determined with a microbalance (Sartorius BP 211D, Germany, accuracy 10 μg).

Characterizations of $V_2O_5 \times H_2O$ Nanoribbon/CC Electrodes: The nanostructure and morphological evolution of the $V_2O_5 \times H_2O$/CC electrodes under different conditions of preparation was examined with a field-emission scanning electron microscope (FESEM, Zeiss Supra 40 VP). To evaluate the growth kinetics, we collected a small amount of $V_2O_5 \times H_2O$/CC electrodes at various stages of the synthesis at intervals

of 6 h and characterized each sample also with FESEM. The dimensions and geometry of $V_2O_5 \times H_2O$ were in addition confirmed by TEM (Philips/FEI CM200, accelerating voltage 200 kV). X-ray powder diffraction (XRD, Stoe STADI-P diffractometer) with Ge-monochromatized Cu-$K_{\alpha1}$ radiation (40 kV, 40 mA) was applied to identify the crystal phase of the specimens. The electrochemical properties of the $V_2O_5 \times H_2O$/CC electrodes were evaluated with CV, GCD methods, and AC impendence analysis. All measurements were performed with a three-electrode system containing the $V_2O_5 \times H_2O$/CC electrode as the working electrode, the Pt foil as the counter-electrode, and a Ag/AgCl electrode as the reference electrode. These evaluations were conducted in aqueous lithium chloride electrolyte.

Fabrication of SSCs: An SSC was built in a two-electrode configuration, in which a membrane separator (PTFE, WL Gore & Associates, soaked with LiCl or PVA/LiCl) was sandwiched between two identical $V_2O_5 \times H_2O$/CC electrodes. Each electrode had the same working area. The dimensions of the fabricated module were 2 cm in length, 0.5 cm in width, and 0.1 cm in height. CV and GCD analyses were adopted to estimate the electrochemical performance. All operating current densities were normalized to the nominal area, namely $1\,\mathrm{cm^2}$, of the symmetric module.

Calculation: The area-normalized capacitances of $V_2O_5 \times H_2O$/CC and VO_x/CC electrodes in aqueous LiCl electrolyte (5 M) were calculated from their CV according to the following equation

$$C_s = \frac{\int I dV}{\nu \Delta V A} \tag{1}$$

in which $C_s/\mathrm{F\,cm^{-2}}$ is the specific capacitance normalized to the effective area; I/A is the current of the discharge curve integrated with respect to the potential V; $\nu/\mathrm{V\,s^{-1}}$ is the charge and discharge rate of the scan; $\Delta V/\mathrm{V}$ is the potential window of the scan; and $A/\mathrm{cm^2}$ is the nominal area of the electrode.

The area-normalized capacitance of a symmetric $V_2O_5 \times H_2O$ supercapacitor was alternatively estimated from the GCD curve with the following equation

$$C_{SSC} = \frac{I}{(\Delta V_{Cell}/\Delta t)A_{Cell}} \tag{2}$$

in which $C_{SSC}/\mathrm{F\,cm^{-2}}$ is the specific capacitance; I/A is the applied current; $\Delta V_{Cell}/\mathrm{V}$ is the cell voltage; $\Delta t/\mathrm{s}$ is the discharge duration after the initial iR drop; and $A_{Cell}/\mathrm{cm^2}$ is the nominal area of the module.

Afterward, the area-normalized energy and power deliveries of the symmetric $V_2O_5 \times H_2O$ supercapacitor were derived from the following formulations

$$E = \frac{1}{2} C_{SSC} \Delta V_{Cell}^2 \times \frac{1000}{3600} \tag{3}$$

$$P = \frac{\Delta V_{Cell}^2}{4 R_{ES} A_{Cell}} \times 1000 \tag{4}$$

in which $E/\mathrm{mW\,h\,cm^{-2}}$ is the energy density normalized to the nominal area of the module; $C_{SSC}/\mathrm{F\,cm^{-2}}$ is the specific capacitance of the module; $\Delta V_{cell}/\mathrm{V}$ is the cell voltage; $P/\mathrm{mW\,cm^{-2}}$ is the power density normalized to the nominal area of the module; $A_{cell}/\mathrm{cm^2}$ is the nominal area of the module; and R_{ES}/Ω is the equivalent series resistance calculated according to the following equation

$$R_{ES} = \frac{\Delta V_{iR}}{2I} \tag{5}$$

in which $\Delta V_{iR}/\mathrm{V}$ is the voltage drop occurring in the galvanostatic charge and the discharge curve if the current polarity was switched and I/A is the applied current.

[1] Z. Yang, J. Zhang, C. W. Kintner-Meyer, X. Lu, D. Choi, J. P. Lemmon, J. Liu, *Chem. Rev.* **2011**, *111*, 3577.

[2] a) D. Pech, M. Brunet, H. Durou, P. Huang, V. Mochalin, Y. Gogotsi, P. -L. Taberna, P. Simon, *Nat. Nanotechnol.* **2010**, *5*, 531; b) J. Chmiola, C. Largeot, P.-L. Taberna, P. Simon, Y. Gogotsi, *Science* **2010**, *328*, 480; c) M. Beidaghi, Y. Gogotsi, *Energy Environ. Sci.* **2014**, *7*, 867; d) S. Y. Lee, K. H. Choi, W. S. Choi, Y. H. Kwon, H. R. Jung, H. C. Shin, J. Y. Kim, *Energy Environ. Sci.* **2013**, *6*, 2414; e) L. Hu, Y. Cui, *Energy Environ. Sci.* **2012**, *5*, 6423; f) J. H. Pikul, H. G. Zhang, J. Cho, P. V. Braun, W. P. King, *Nat. Commun.* **2013**, *4*, 1732.

[3] a) L. Li, J. Zhang, Z. Peng, Y. Li, C. Gao, Y. Ji, R. Ye, N. D. Kim, Q. Zhong, Y. Yang, H. Fei, G. Ruan, J. M. Tour, *Adv. Mater.* **2016**, *28*, 838; b) M. F. El-Kady, M. Ihns, M. Li, J. Y. Hwang, M. F. Mousavi, L. Chaney, A. T. Lech, R. B. Kaner, *Proc. Natl. Acad. Sci. USA* **2015**, *112*, 4233; c) T. M. Dinh, A. Achour, S. Vizireanu, G. Dinescu, L. Nistor, K. Armstrong, D. Guay, D. Pech, *Nano Energy* **2014**, *10*, 288; d) H. Xu, X. Hu, Y. Sun, H. Yang, X. Liu, Y. Huang, *Nano Res.* **2015**, *8*, 1148; e) A. Ferris, S. Garbarino, D. Guay, D. Pech, *Adv. Mater.* **2015**, *27*, 6625; f) M. B. Sassin, C. N. Chervin, D. R. Rolison, J. W. Long, *Acc. Chem. Res.* **2013**, *46*, 1062.

[4] a) Y. C. Chen, Y. G. Lin, Y. K. Hsu, S. C. Yen, K. H. Chen, L. C. Chen, *Small* **2014**, *10*, 3803; b) M. B. Sassin, A. N. Mansour, K. A. Pettigrew, D. R. Rolison, J. W. Long, *ACS Nano* **2010**, *4*, 4505; c) Y. K. Hsu, Y. C. Chen, Y. G. Lin, L. C. Chen, K. H. Chen, *J. Power Sources* **2013**, *242*, 718; d) J. Zhang, J. Wang, J. Yang, Y. Wang, M. B. Chan-Park, *ACS Sustainable Chem. Eng.* **2014**, *2*, 2291.

[5] P. Simon, Y. Gogotsi, B. Dunn, *Science* **2014**, *343*, 1210.

[6] a) Y. Gogotsi, P. Simon, *Science* **2011**, *334*, 917; b) S. Zhang, N. Pan, *Adv. Energy Mater.* **2015**, *5*, 1401401.

[7] M. F. El-Kady, V. Strong, S. Dubin, R. B. Kaner, *Science* **2012**, *335*, 1326.

[8] a) Z. L. Wang, *Adv. Mater.* **2012**, *24*, 280; b) J. G. Koomey, H. S. Matthews, E. Williams, *Annu. Rev. Environ. Resources* **2013**, *38*, 311.

[9] a) J. C. Lytle, J. M. Wallace, M. B. Sassin, A. J. Barrow, J. W. Long, J. L. Dysart, C. H. Renninger, M. P. Saunders, N. L. Brandell, D. R. Rolison, *Energy Environ. Sci.* **2011**, *4*, 1913; b) B. L. Ellis, P. Knauth, Thierry Djenizian, *Adv. Mater.* **2014**, *26*, 3368; c) J. Lin, C. Zhang, Z. Yan, Y. Zhu, Z. Peng, R. H. Hauge, D. Natelson, J. M. Tour, *Nano Lett.* **2013**, *13*, 72.

[10] A. E. Fischer, K. A. Pettigrew, D. R. Rolison, R. M. Stroud, J. W. Long, *Nano Lett.* **2007**, *7*, 281.

[11] K. Jost, C. R. Perez, J. K. McDonough, V. Presser, M. Heon, G. Dion, Y. Gogotsi, *Energy Environ. Sci.* **2011**, *4*, 5060.

[12] a) T. Zhai, X. Lu, Y. Ling, M. Yu, G. Wang, T. Liu, C. Liang, Y. Tong, Y. Li, *Adv. Mater.* **2014**, *26*, 5869; b) L. Li, S. Peng, H. B. Wu, L. Yu, S. Madhavi, X. W. Lou, *Adv. Energy Mater.* **2015**, *5*, 1500753; c) S. Fleischmann, N. Jackel, M. Zeiger, B. Kruner, I. Grobelsek, P. Formanek, S. Choudhury, D. Weingarth, V. Presser, *Chem. Mater.* **2016**, *28*, 2802; d) Q. Qu, S. Yang, X. Feng, *Adv. Mater.* **2011**, *23*, 5574.

[13] H. G. Bachmann, F. R. Ahmed, W. H. Barnes, *Z. Kristallogr.* **1961**, *115*, 110.

[14] I. Nam, G. P. Kim, S. Park, J. W. Han, J. Yi, *Energy Environ. Sci.* **2014**, *7*, 1095.

[15] J. Livage, *Materials* **2010**, *3*, 4175.

[16] G. Wang, X. Lu, Y. Ling, T. Zhai, H. Wang, Y. Tong, Y. Li, *ACS Nano* **2012**, *6*, 10296.

[17] G. E. Walrafen, *J. Chem. Phys.* **1964**, *40*, 3249.

[18] R. Baddour-Hadjean, J. P. Pereira-Ramos, *Chem. Rev.* **2010**, *110*, 1278.

[19] Y. Repelin, E. Husson, L. Abello, G. Lucazeau, *Spectrochim. Acta* **1985**, *41A*, 993.

[20] V. Augustyn, P. Simon, B. Dunn, *Energy Environ. Sci.* **2014**, *7*, 1597.

[21] Y. Shao, M. F. El-Kady, J. Sun, Y. Li, Q. Zhang, M. Zhu, H. Wang, B. Dunn, R. B. Kaner, *Chem. Rev.* **2018**, *118*, 9233.

[22] a) M. B. Sassin, A. N. Mansour, K. A. Pettigrew, D. R. Rolison, J. W. Long, *ACS Nano* **2010**, *8*, 4505; b) Y. K. Hsu, Y. C. Chen, Y. G. Lin, L. C. Chen, K. H. Chen, *Chem. Commun.* **2011**, *47*, 1252; c) Y. K. Hsu, Y. C. Chen, Y. G. Lin, *Electrochim. Acta* **2014**, *139*, 401.

[23] D. Wei, M. R. J. Scherer, C. Bower, P. Andrew, T. Ryhanen, U. Steiner, *Nano Lett.* **2012**, *12*, 1857.

[24] a) Y. Yang, Q. Huang, L. Niu, D. Wang, C. Yan, Y. She, Z. Zheng, *Adv. Mater.* **2017**, *29*, 1606679; b) B. Yao, S. Chandrasekaran, J. Zhang, W. Xiao, F. Qian, C. Zhu, E. B. Duoss, C. M. Spadaccini, M. A. Worsley, Y. Li, *Joule* **2019**, *3*, 459; c) X. Zhang, D. Su, A. Wu, H. Yan, X. Wang, D. Wang, L. Wang, C. Tia, L. Sun, H. Fu, *Sci. China Mater.* **2019**, *62*, 1115.

[25] a) P. Huang, D. Pech, R. Lin, J. K. McDonough, M. Brunet, P. -L. Taberna, Y. Gogotsi, P. Simon, *Electrochem. Commun.* **2013**, *36*, 53; b) T. M. Dinh, K. Armstrong, D. Guay, D. Pech, *J. Mater. Chem. A* **2014**, *2*, 7170; c) X. Wang, Y. Yin, X. Li, Z. You, *J. Power Sources* **2014**, *252*, 64; d) C. Yang, L. Zhang, N. Hu, Z. Yang, H. Wei, Y. Zhang, *J. Power Sources* **2016**, *302*, 39.